

# Manifold death: a Volume of Fluid implementation of controlled topological changes in thin sheets by the signature method

Leonardo Chirco<sup>a,\*</sup>, Jacob Maarek<sup>a</sup>, Stéphane Popinet<sup>a</sup>, Stéphane Zaleski<sup>a,b</sup>

<sup>a</sup>*Sorbonne Université and CNRS, Institut Jean Le Rond d'Alembert UMR 7190, F-75005 Paris, France*

<sup>b</sup>*Institut Universitaire de France, Paris, France*

---

## Abstract

A well-known drawback of the Volume-Of-Fluid (VOF) method is that the breakup of thin liquid films or filaments is mainly caused by numerical aspects rather than by physical ones. The rupture of thin films occurs when their thickness reaches the order of the grid size and by refining the grid the breakup events are delayed. When thin filaments rupture, many droplets are generated due to the mass conserving properties of VOF. Thus, the numerical character of the breakup does not allow obtaining the desired convergence of the droplet size distribution upon grid refinement. In this work, we present a novel algorithm to detect and perforate thin structures. First, thin films or ligaments are identified by taking quadratic moments of an indicator obtained from the volume fraction. A multiscale approach allows us to choose the critical film thickness independently of the mesh resolution. Then, the breakup is induced by making holes in the films before their thickness reaches the grid size. We show that the method improves the convergence upon grid refinement of the droplets size distribution and of enstrophy.

*Keywords:* Two-phase flows, Volume of fluid, Breakup, Topology changes

---

## 1. Introduction

Multiphase fluid mechanics with sharp interfaces involves diverse singularities each with its own difficulties. In this paper we address the change of topology happening when a hole forms in a thin liquid sheet and in particular its numerical modelling in Volume-Of-Fluid (VOF) methods. This topology change has important consequences for fluid fragmentation, and in particular for the droplet size distribution. Several mechanisms for the rupture of thin sheets have been proposed [1, 2], but a full description is still missing. In some cases, inter-molecular forces may be shown to have a destabilizing effect on thin sheets, while in other cases, as in some soap films, permanent dipoles may form on interfaces having a stabilizing effect [3]. In this paper we consider interfaces that do not display such a stabilizing effect and break before reaching molecular length scales.

Mathematically, the Navier-Stokes equations with the assumption of sharp interfaces between phases are incomplete as they do not describe the piercing of thin sheets. These equations can only describe the indefinite thinning of a sheet when it is compressed or stretched by the flow. Eventually, it may happen that the sheet becomes thinner than molecular scales, at which point the equations cease to be valid. However, before this happens, molecular forces may induce the breakup of films [4, 5, 6, 7, 8]. In many cases, however, and in particular in atomization or floating bubble experiments, observations show that sheets are pierced well before their thickness reaches molecular length scales [9, 10]. Thus, an ad-hoc prescription for piercing thin sheets of some macroscopic length scale is needed to describe real flows.

---

\*Corresponding author

*Email addresses:* [leonardo.chirco@sorbonne-universite.fr](mailto:leonardo.chirco@sorbonne-universite.fr) (Leonardo Chirco), [jacob.maarek@sorbonne-universite.fr](mailto:jacob.maarek@sorbonne-universite.fr) (Jacob Maarek), [popinet@basilisk.fr](mailto:popinet@basilisk.fr) (Stéphane Popinet), [stephane.zaleski@sorbonne-universite.fr](mailto:stephane.zaleski@sorbonne-universite.fr) (Stéphane Zaleski)

In addition to the physical modelling challenge, the numerical simulation of thin sheets and their breakup poses significant challenges. In fact, when the fluid structures become too thin they can not be correctly resolved with the Volume-of-Fluid (VOF) method. The most popular interface reconstruction approaches are responsible for the breakup of thin sheets whose thickness is of the order of the grid size and for the formation of several droplets. To avoid the occurrence of artificial breakup using VOF, extremely fine grids must be used, such that  $\Delta < h$  (where  $\Delta$  is the cell size and  $h$  the film thickness) and huge computational efforts are required even using codes with adaptive mesh refinement (AMR) capabilities [11, 12]. Otherwise, as soon as the thickness of the liquid sheet approaches the cell size ( $\Delta \approx h$ ), the artificial breakup of thin sheets does not permit to observe convergence upon grid refinement of some meaningful quantities such as the droplets size distribution or enstrophy. The standard Level-Set (LS) method [13] does not guarantee mass conservation and mass/volume evaporation occurs when the filaments become thinner than the cell size. Thus, various techniques, such as particle LS [14, 15] or mass conserving LS [16] have been developed to reduce this limitation. Anyhow, an intrinsic breakup length scale (equal to the grid size or smaller, depending on the LS method) exists and the rupture of thin structures with high curvature is still dependent on the grid size. Finally, Front-Tracking (FT) [17] methods do not include automatic topology modification and breakup/reconnection algorithms must be implemented.

Some methods have been proposed to detect thin ligaments or sheets. In [18] a Multimaterial Moment-of-Fluid method is used to capture under-resolved filaments thinner than the grid cells, while a two-plane reconstruction to track sub-grid scale sheets has been recently proposed in [19]. A geometric approach is used in [20] to detect the medial axis in a Level-Set framework. Automatic reconnection algorithms have been suggested for thin sheets in the Front-Tracking method [21]. A limitation of the work is that the authors decide to use a critical reconnection thickness proportional to the cell size and therefore the breakup process remains grid-dependent. Some algorithms have also been suggested to make “numerical” reconnection impossible for the VOF method [22]. We are not aware of any similar mechanisms (either promoting reconnection or blocking it) for the Level-Set method.

In this paper we propose a *manifold death* algorithm to perforate sheets or ligaments of a given thickness in a controlled way, thus avoiding the numerical breakup that affects the VOF method and the associated grid convergence issues. First, the thin regions are detected by computing quadratic forms based on the values of the color function. The signs of the eigenvalues of the quadratic form, known as *signature*, are then used to identify thin regions. Once their position is known, we want to create artificial holes that expand and “destroy” the thin regions. This leads to several questions, such as: how many holes are needed to perforate a thin sheet, where are they placed, when do they appear? However, these are still open questions. In fact, many complex phenomena are involved in the physics of hole nucleation that leads to the rupture of thin sheets, see [2]. For example, in the experiments of [23] one or several holes are seen but their origin is still not known nor is the effect of the number of holes investigated. With this in mind, when developing the manifold death method, to answer the prior questions we tried to maintain a balance between the ambition to replicate the observations and a feasible numerical implementation. This work has to be intended as a preliminary study, in particular about the hole formation aspects and parameters, and further improvements and comparisons will be performed in the future.

The rest of the paper is organized as follows. The mathematical model is defined in Section 2. The manifold death algorithm is described in Section 3. The numerical results obtained with the manifold death algorithm are discussed in Section 4, followed by our conclusions.

## 2. Governing equations

The governing equations for the incompressible two-phase flow with immiscible fluids are written using the one-fluid formulation, see [24]. A Heaviside function  $H$  is used to locate the interface, such that  $H = 1$  in fluid 1 and  $H = 0$  elsewhere. To solve numerically the problem, the discontinuous  $H$  function is replaced with the discretized volume fraction (or color function)  $C$  defined as the average value of  $H$  in each computational cell. The volume fraction  $C$  is then a piece-wise constant approximation of  $H$  such that  $C \in [0, 1]$ , where fractional values are associated to the cells cut by the interface. Then, in the one-fluid formulation, the

value of a generic material property  $\pi$  is a function of  $C$ , namely  $\pi = C\pi_1 + (1 - C)\pi_2$ . The volume fraction is obtained by solving the following advection equation

$$\frac{\partial C}{\partial t} + \mathbf{u} \cdot \nabla C = 0. \quad (1)$$

The velocity  $\mathbf{u}$  and pressure  $p$  are obtained by solving the Navier-Stokes equations that express the conservation of mass and momentum

$$\frac{\partial \rho \mathbf{u}}{\partial t} + \nabla \cdot (\rho \mathbf{u} \mathbf{u}) = -\nabla p + \nabla \cdot [\mu (\nabla \mathbf{u} + \nabla \mathbf{u}^T)] + \rho \mathbf{g} + \mathbf{f}, \quad (2)$$

$$\nabla \cdot \mathbf{u} = 0, \quad (3)$$

where  $\rho$  and  $\mu$  are the density and viscosity, respectively. The gravitational force is taken into account with the  $\rho \mathbf{g}$  term. Surface tension is modeled with the term  $\mathbf{f} = \sigma \kappa \mathbf{n} \delta_S$ , where  $\sigma$  is the surface tension,  $\kappa$  denotes the curvature of the interface,  $\mathbf{n}$  is the unit vector normal to the interface and  $\delta_S$  is the surface Dirac distribution on the interface (i.e. zero everywhere except on the interface).

The open-source code Basilisk is used to solve the two-phase incompressible Navier-Stokes system with quad/octrees [25]. An efficient adaptive technique based on a wavelet decomposition of the volume fraction and velocity fields allows solving with a high resolution only in the relevant parts of the domain, thus reducing the computational cost of the simulation [26]. A momentum-conserving scheme is used for the velocity. A piece-wise linear geometric VOF method is adopted for tracking the interface and a well-balanced Continuous Surface Force (CSF) method coupled with height functions is used to calculate the surface tension term [27].

### 3. The manifold death algorithm

In this section we describe the manifold death method used to perforate thin structures in a controlled way.

#### 3.1. The signature method

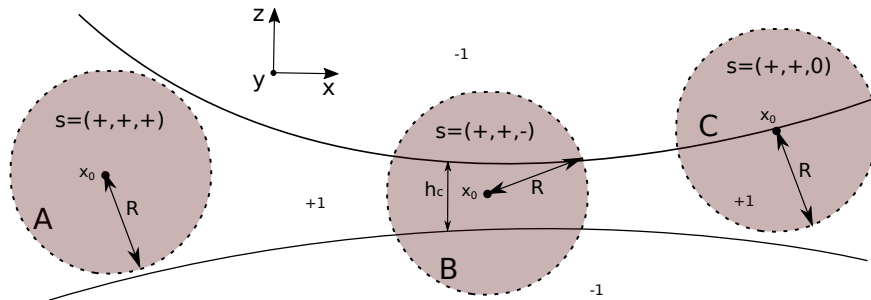


Figure 1: Graphical representation of the signature method applied to a sheet infinite in the  $y$  direction. A: bulk of phase. B: thin sheet. C: interface.

The first step of the manifold death algorithm consists in detecting the thin sheets (or ligaments) in the domain. To do that, we use the following *signature method*:

1. Consider a point  $\mathbf{x}_0 \in \mathbb{R}^3$  and translate the coordinate system so that the new origin is  $\mathbf{x}_0 = \mathbf{0}$ . Consider a radius  $R$  approximately the same size of the sheet thickness  $h_c$  one wants to detect, see Figure 1, and the bilinear form  $f(\mathbf{x}, \mathbf{x}) = x_i x_j T_{ij}$ .
2. The quadratic moments  $T_{ij}$  on a sphere  $S$  of radius  $R$  can be found by integrating

$$T_{ij} = \int_V x'_i x'_j \phi(\mathbf{x}') d\mathbf{x}', \quad (4)$$

where  $\phi = 2C - 1$  is a symmetric indicator function.

---

**Algorithm 1** The signature method

1. Set  $\phi = 2C - 1$ .

▷ *Symmetric indicator function*
**for all cells do**

2. Translate the coordinates as  $x_i \leftarrow x_i - x_{cell}$  with  $i = 1, \dots, 3$ .

3. Compute the quadratic moments  $T_{ij}$  using Eq. (4).

4. Compute the eigenvalues  $\epsilon_i$  of  $\mathbf{T}$  to build the signature  $s$ .

5. Locate the cell using Table 1.

**end for**


---

Signature $s$		Position of $\mathbf{x}_0$
3D	2D	
(+, +, +)	(+, +)	Bulk of the phase
(+, +, -)	/	Sheet
(+, -, -)	(+, -)	Ligament
(+, +, 0)	(+, 0)	Interface
(+, -, 0)	/	Edge of a sheet
(-, -, 0)	(-, 0)	Edge of a ligament

Table 1: Examples of the signature in three and two dimensions, see Figure 1.

3. After orthonormalization of the quadratic form, one finds a new set of coordinates in which  $f(\mathbf{X}, \mathbf{X}) = \epsilon_i X_i^2$ , where  $\epsilon_i$  are the eigenvalues of the operator with matrix  $\mathbf{T}$ . The number of positive, negative and zero values of  $\epsilon_i$  is the signature  $s$  of the quadratic form. For the given point  $\mathbf{x}_0$ , the signature  $s$  indicates the average shape of the interface in the vicinity of the point and can be used to determine whether the point is in the bulk of the phase, in a thin sheet (or ligament) or close to the interface, see Figure 1 and Table 1.

The eigenvalues of  $\mathbf{T}$  can be found by solving the equation

$$\det(\mathbf{T} - \epsilon \mathbf{I}) = 0, \quad (5)$$

that in two dimensions gives  $\epsilon_{1,2} = \text{tr}(\mathbf{T}) \pm \sqrt{(\text{tr}(\mathbf{T})^2 - 4\Delta)}/2$ . For computing the eigenvalues, we rely on the GNU Scientific Library [28]. Table 1 lists some of the signatures that can be obtained using this method, while a concise description of the signature method is given in Algorithm 1.

To clarify the rationale for the signatures reported in Table 1, let us introduce the following example. Consider a sheet aligned with the axis, infinite in the  $y$  direction and of thickness  $h_c$  in the  $z$  direction, see Figure 1. We first recall that the signature of a matrix is invariant upon rotation of the coordinate system. From symmetry, the non-diagonal terms of  $\mathbf{T}$  cancel out or are negligible for a slightly deformed object and only the diagonal terms remain:  $T_{xx}, T_{yy}, T_{zz} = \int x_i'^2 \phi(\mathbf{x}') d\mathbf{x}'$ , which means that we are integrating along the Cartesian axis. These remaining diagonal terms are the eigenvalues of  $\mathbf{T}$  and their signs are the signature we are interested in. When we evaluate  $T_{xx} = \int x'^2 \phi(\mathbf{x}') d\mathbf{x}'$ , since we are inside phase 1 we have  $C = 1$  and  $\phi = 1$  so that  $T_{xx}$  is positive. The same arguments can be used to show that also  $T_{yy} = \int y'^2 \phi(\mathbf{x}') d\mathbf{x}'$  is positive. When we consider  $T_{zz} = \int z'^2 \phi(\mathbf{x}') d\mathbf{x}'$ , if we use for the integration a sphere of radius  $R < h_c/2$  (sphere A in Figure 1), we are again inside the reference phase,  $T_{zz} = 1$ , and we recover the signature (+, +, +) typical of the bulk of phase. If instead we take  $R > h_c/2$  (sphere B in the same figure), we are no longer in the reference phase so  $C = 0$ ,  $\phi = -1$ ,  $T_{zz}$  is negative and the signature (+, +, -) identifies a thin sheet. For a ligament (consider doing a revolution around the horizontal axis of Figure 1) aligned with one of the axis (e.g. the  $x$  one), the signature becomes (+, -, -), since the integration of  $T_{yy}$  now yields a negative value. Finally, zero values are obtained when the center of the sphere used for the integration lies on the interface (sphere C in the same figure), since the positive and negative contributions cancel out. Then the signature (+, -, 0) denotes the edge of a sheet, while (-, -, 0) the edge of a ligament. From a numerical point of view, we use a heuristically chosen threshold (0.1) to detect zero eigenvalues. The thin

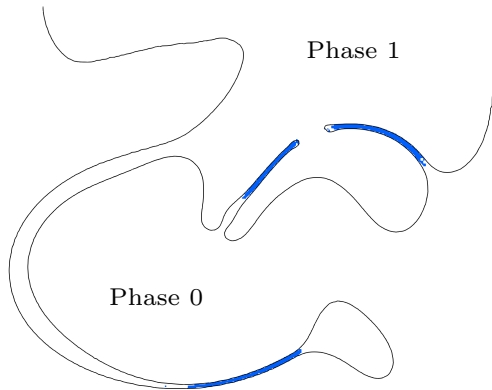


Figure 2: Slice of a 3D simulation. Interface in black and thin sheets in blue.

sheets identified with the signature method are shown in Figure 2. The figure clearly shows that the method is symmetric. In fact, the algorithm detects a thin sheet in the reference phase in the bottom, while, in the two other regions above, the reference phase 1 encloses thin sheets of the phase 0. To summarize, with this method we can identify thin regions in both phases.

### 3.2. Basilisk implementation

For the numerical computation of the quadratic moments in (4), some simplifications and adjustments are necessary to tailor the method to the Basilisk code. For simplicity, we first replace the sphere with a cube centered in  $\mathbf{x}_0$  of size  $L = 2R$ . The numerical integration of (4) is done on a shell of thickness  $\Delta$ , the hatched cells in Figure 3. Moreover, in order to take advantage of Basilisk’s capabilities, we make sure that the cube lies completely within the stencil (i.e. the set of surrounding cells) around  $\mathbf{x}_0$ . Since the standard stencil size in Basilisk is five cells ( $5\Delta$ ), we can detect thin sheets whose thickness is approximately three cells ( $3\Delta$ ). To identify larger sheets ( $h_c > 3\Delta$ ) we take advantage of the multilevel nature of Basilisk by computing the signature on the appropriate coarser grid. In fact, after the first step of Algorithm 1, we restrict the values of  $\phi$  to the appropriate coarser grid and, at the end of the algorithm, we prolongate back the obtained signatures onto finer grids. The restriction operator used for the indicator function  $\phi$  sets to the coarse *parent* cells the average value of the four (eight in 3D) corresponding *children* cells. The prolongation operator for the signature simply attributes to the children cells the value of their parent cell. Therefore, a critical thin sheet thickness can be set independently from the mesh resolution. Figure 3 illustrates the multilevel approach used for detecting thin structures. Using the finer grid (left), the distance between the two interfaces is larger than  $h_c \approx 3\Delta_{fine}$  and the shaded cell is marked as “bulk of phase”, while on the coarser one a thin structure of thickness  $h_c \approx 3\Delta_{coarse} = 6\Delta_{fine}$  is detectable.

We would like to remark that the algorithm is compatible with the adaptive-grid approach of Basilisk and then it is suitable for large parallel computation. Also, our observations indicate that the computational time required for computing the signature is small compared to the time used by the multiphase solver to advance the solution. In Table 2 we give the CPU time for ten time steps of the multiphase solver with and without the signature method. For these measurements, we take our last numerical test (phase inversion, Section 4.3) using a  $512^3$  maximum resolution and the signature is computed with three different  $h_c$ . The computational overhead introduced by the signature method ranges from 1.9% to 7.2% of the reference time. By considering larger  $h_c$  the overhead reduces, since the number of active cells becomes smaller. This is due to the use of the multilevel approach on adaptive octree grids, in fact, with every restriction operation, groups of eight children cells are replaced by one common parent cell. Moreover, the full manifold death algorithm (of which the signature method is the first step) should not be invoked at every time step (see Section 3.3) and then the computational overhead attributable to the signature method can be considered negligible.

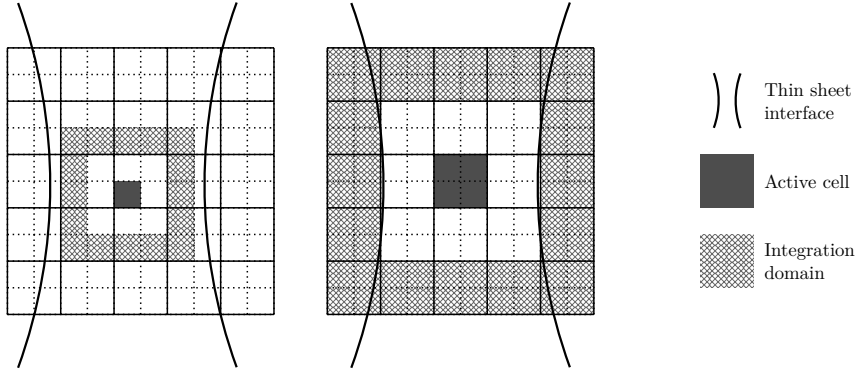


Figure 3: Multilevel implementation of the signature method. Domains used for the numerical integration of (4) (hatched cells) on a fine (left) and coarse (right) grid around the shaded active cell  $\mathbf{x}_0$ . The detectable critical thickness  $h_c$  on the coarse grid (right) is twice the one on the finer grid (left).

Finally, the signature method can be used also as a criterion to enforce adaptive grid refinement in thin regions, see [29].

Test case	CPU time (s)	Relative CPU	Nb active cells
Multiphase solver	74.06	1	1 825 064
$h_{c1} = 3\Delta_{128}$	75.46	1.019	406 840
$h_{c2} = 3\Delta_{256}$	77.26	1.043	1 180 664
$h_{c3} = 3\Delta_{512}$	79.40	1.072	1 825 064

Table 2: CPU time and number of active cells for the reference case without signature method and with the signature method with three values of thin sheet thickness  $h_c$ .  $\Delta_N$  is equal to  $L/N$ , where  $L$  is the domain size and  $N$  the number of cells per side.

### 3.3. The topology changes

---

**Algorithm 2** The creation of holes

---

**Require:** The signature  $\epsilon$  for every cell.

**for all** cells belonging to thin regions **do**

1. Randomly choose the position of the holes.  $\triangleright$  Create at most  $n_h$  holes

**if** cell to perforate **then**

2. Compute average  $C$  in the stencil around cell.

**if**  $C < C^*$  **then**

3.  $C = 1$ .  $\triangleright$  Holes made in phase 0

**else**

4.  $C = 0$ .  $\triangleright$  Holes made in phase 1

**end if**

**end if**

**end for**

5. Advance the solution by  $t_h$  before calling again this algorithm.

---

Once we have identified the thin sheets with the signature method, we want to perforate them by creating holes before their thickness reaches the cell size and the numerical breakup happens. Since a universal theory for the film breaking mechanism has not yet been developed (see [2]), we decide to select randomly the cells (among those in thin sheets) where a hole is created.

For this part of the manifold death method we need to introduce many parameters whose values have been chosen empirically. More sophisticated versions and a broader investigation of the effect of these parameters on the method will be presented in future works. When the previously detected thin regions are in the reference phase (i.e.  $C > C^*$ ), we change the topology by placing some cubic holes setting the color function  $C$  to zero. Otherwise, to force interface reconnections when the thin region is in the other phase ( $C < C^*$ ), we set the color function  $C$  to 1. In our simulations we take  $C^* = 0.3$ .

An important remark is that the size of the holes (made in both phases) is critical, in fact holes will expand only if their diameter is at least the sheet thickness  $h_c$ , otherwise they will re-close to minimize the energy of the system [30]. In order to recover the desired grid independency, in addition to the thickness  $h_c$ , also the size of the holes has to be fixed and independent of the cell size. To this aim, we create cubic holes of the same length  $h_c$  used for the computation of the signature. By choosing the minimum size for which the expansion criterion is satisfied, we are minimizing the perturbations on the system as well as the amount of mass removed or added. Similarly, we want to minimize the number of holes that we create, since they have an impact on the overall dynamics of the retracting rim. Thus, the manifold death algorithm is used only at fixed time interval  $t_h$  to give the holes some time to expand with Taylor-Culick velocity and we limit the maximum number of holes  $n_h$  created at every iteration. In the limit where the manifold death is used at every iteration of the multiphase solver, which means that  $t_h$  is equal to the presumably small time step, the holes do not have enough time to expand and the thin sheets gets replaced by a large number of holes in an unphysical manner. On the contrary, if  $t_h$  is too large the unwanted numerical breakup happens. A description of the method is reported in Algorithm 2.

## 4. Results

In this section we present our results. We apply the manifold death method to a simple single vortex test, to an axisymmetric secondary atomization situation and to a phase inversion problem.

### 4.1. Single vortex

The single vortex test has been designed to check the ability of interface tracking methods when the reference phase undergoes large deformations and thin structures of thickness of the same order of the grid size are involved, see [31, 32]. For this test, the surface tension is set to zero. The divergence-free velocity  $\mathbf{u} = (u_x, u_y)$  is obtained from the following stream function

$$\psi = \frac{1}{\pi} \sin^2(\pi x) \sin^2(\pi y), \quad (6)$$

as  $u_x = \partial\psi/\partial y$  and  $u_y = -\partial\psi/\partial x$ . The domain is a unit square with the bottom left corner placed in the origin and a circular droplet with radius  $r = 0.15$  is centered at  $(0.5, 0.75)$ . On the sides of the box, homogeneous Dirichlet boundary conditions are imposed. The rotation ends at  $T = 3$  s.

We use this simple test to check the first step of the manifold death algorithm, namely the detection of thin structures where the artificial breakup occurs. If we perform the simulation on a coarse mesh we observe a certain amount of artificial breakup events and, if we move to finer grids, we expect to obtain fewer breakup events, as the filament remains larger than the grid size for a longer time. Since we aim to tackle the problem of the non-convergence upon grid refinement, we first show that our method can replicate on finer grids (in a controlled fashion) what happens numerically on a coarse grid taken as reference. In other words, we check if the manifold death method is able to identify and perforate the ligament on finer grids as soon as it reaches a thickness equal to the reference coarse grid size. To do so, the critical ligament thickness  $h_c$  used in the algorithm has to be equal to the grid size  $\Delta_l$  of the coarse mesh. This requires  $\Delta_l = h_c \approx 3\Delta_{l+1}$ , where  $\Delta_{l+1}$  indicates the finer grid size. However, using the standard multilevel,  $\Delta_l = 2\Delta_{l+1}$  holds true and since Basilisk uses quadtree grids, which restricts the number of cells per side to powers of two, the simpler way to satisfy this requirement is to increase the coarse grid size  $\Delta_l$  by taking a square domain of size 1.5 (note that this would be equivalent to using a  $47^2$  grid on the unit square).

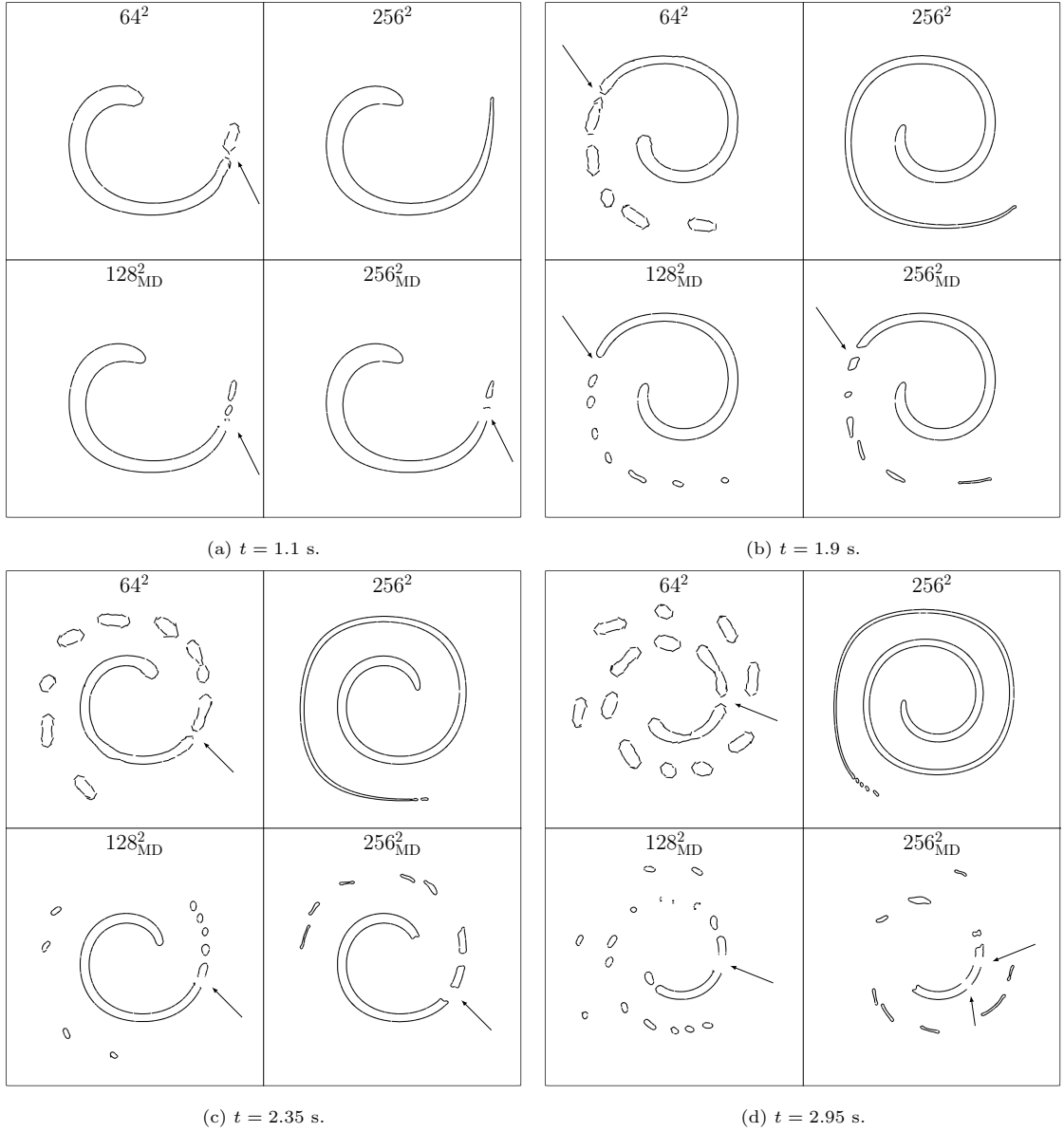


Figure 4: Position of the interface at various instants for the single vortex test. In each frame the following cases are shown:  $64^2$  (top left) and  $256^2$  (top right) grids without controlled perforation,  $128^2$  (bottom left) and  $256^2$  (bottom right) grids with manifold death. The arrows indicate the position of the latest breakup.

We show in Figure 4 the interface at different grid resolutions with and without manifold death. The four sub-pictures correspond to different times. In the top row of each picture we report the interface with no manifold death for the  $64^2$  (used as reference) and  $256^2$  (only reported as a comparison) grids, while in the bottom row the manifold death method is used with constant  $h_c = 0.023m = 3\Delta_{128}$  on the  $128^2$  and  $256^2$  grids. Note that, for clarity, the smallest droplets have been removed. The criterion used for the mesh adaptation is the error on the volume fraction field  $C$  with a threshold equal to  $1 \cdot 10^{-5}$ . The frequency of holes creation is  $t_h = 0.05$  s and the maximum number of holes per manifold death call is  $n_h = 10$ .

Using the standard VOF the breakup of the thin filament is clearly grid dependent, since with the coarser ( $64^2$ ) grid at the end of the simulation the reference phase is made of a set of droplets, while with the finer



(256<sup>2</sup>) one the thin filament is still well resolved and only few droplets have been created near the end of the tail. The validation of the manifold death method, and in particular the detection of thin structures, can be done qualitatively by comparing the position of the most recent breakup event (indicated by the arrows) for the two cases with manifold death and for the 64<sup>2</sup> case without controlled perforation. By controlling the breakup, we have replicated on finer grids what happens numerically on a coarser grid, showing that the method accurately detects and perforates thin structures of given thickness independently of the grid resolution used.

#### 4.2. Secondary atomization

Secondary atomization refers to the physical situation where the droplets originated from the primary atomization of a jet, due to the interaction with the ambient high speed gas flow, deform and fragment. Here, we study the evolution of a single droplet that experiences an impulsive acceleration of the surrounding gas. The droplet is initially at rest, surrounded by fluid with zero velocity. At  $t = 0$  an impulsive velocity  $U_0$  condition is imposed on the left boundary. The drop then stretches and deforms into a film whose shape resembles that of a bag. As the bag inflates, its thickness decreases until holes appear and the bag breaks up bursting the bag into a spray. An extensive analysis of the different fragmentation regimes that the droplets may experience has been carried out in [33, 34, 35]. The goal of this paper is not to further investigate the secondary atomization problem, instead we want to show the improvements in terms of grid convergence that can be attained using the manifold death method. To this aim, we select a single case from [35] with the intent to show that we are able to control the sheet breakup, while in the standard VOF simulations it happens numerically as soon as the sheet thickness reaches the minimal grid size.

The computational domain is a two-dimensional axisymmetric channel, represented by a square of side  $15R_0$ , where  $R_0$  is the droplet initial radius used in the adimensionalization. The dynamics of the droplet can be uniquely determined by the Reynolds  $Re = \rho_G U_0 R_0 / \mu_G$  and Weber  $We = \rho_G R_0 U_0^2 / \sigma$  numbers, the ratio of densities  $r_d = \rho_L / \rho_G$  and the ratio of viscosities  $r_v = \mu_L / \mu_G$ . For this test we take  $Re = 1090$ ,  $We = 7.5$ ,  $r_d = 1110$  and  $r_v = 90.9$ . We perform the simulations on three fine grids 8192<sup>2</sup>, 16384<sup>2</sup> and 32768<sup>2</sup> (corresponding to the levels of refinement 13, 14 and 15) with up to 2000 cells per droplet radius. Adaptation is performed using a threshold of  $10^{-5}$  and  $5 \cdot 10^{-5}$  on the velocity  $\mathbf{u}$  and volume fraction  $C$  errors, respectively. For this test case we set  $t_h = 0.1$  and impose that only one hole is done during the whole simulation. To reduce the effects of the long initial transient where the droplet stretches and forms the forward-facing bag, we start the simulations on the finer grid by using a snapshot obtained at lower resolution. Figure 5 shows the evolution of the droplet until its breakup for the different grids. The droplet

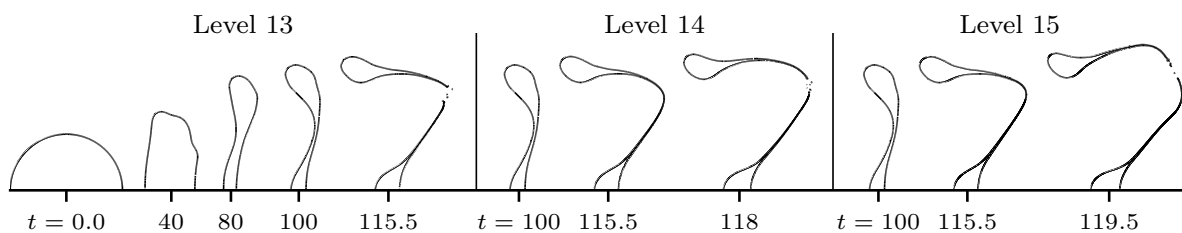


Figure 5: Drop deformation and breakup without manifold death (non controlled) for three grid resolutions.

deforms and a forward facing bag is formed. The breakup occurs at  $t = 115.0$  at the lower resolution and at  $t = 119.2$  when using the finer grid, see Table 3. The evolution is similar to the one in [35], apart from the bulge near the symmetry axis that was not observed in the previous work.

The breakup of the droplet is shown in Figure 6 for the coarsest and finest grids. The black line indicates the interface when the manifold death (MD) method is used, while the gray background shows the position of the deformed droplet in the case with non controlled breakup (NC) at the same mesh resolution. From top to bottom, we report the results obtained reducing the critical thickness  $h_c$  at which thin sheets are detected and perforated. In the top row we set  $h_{c1} = 3\Delta_{2048} = 0.022R_0$ , in the middle one  $h_{c2} = 3\Delta_{4096}$

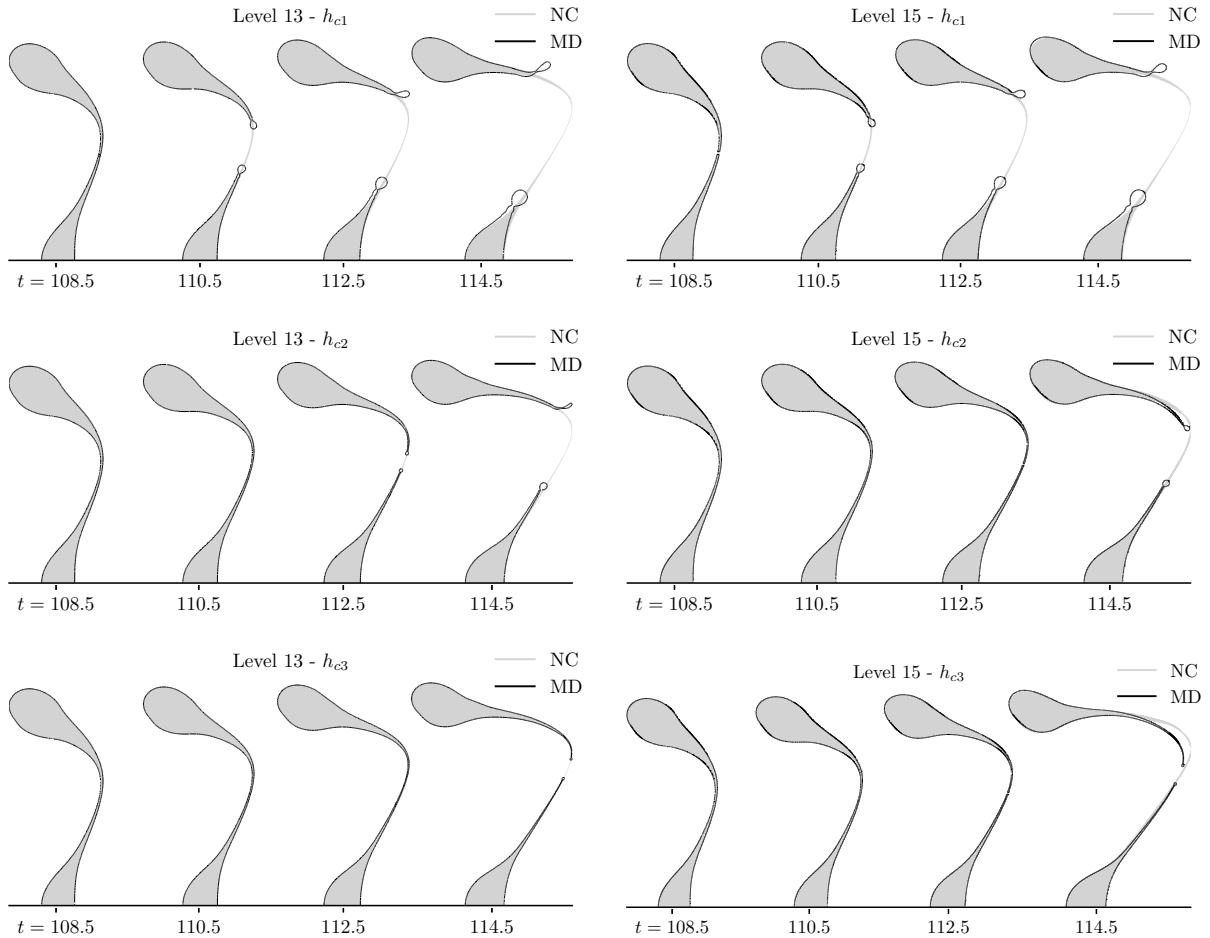


Figure 6: Drop deformation using the  $8192^2$  (Level 13, left) and  $32768^2$  grids (Level 15, right). The black line shows the position of the interface when the manifold death (MD) method is used, while the gray background shows the droplet position with non controlled (NC) breakup. The critical thickness ranges from  $h_{c1} = 3\Delta_{2048}$  (top) to  $h_{c2} = 3\Delta_{4096}$  (center) and  $h_{c3} = 3\Delta_{8192}$  (bottom).  $\Delta_N$  is equal to  $L/N$ , where  $L$  is the domain size and  $N$  the number of cells per side.

and, finally, in the bottom one  $h_{c3} = 3\Delta_{8192}$ . Table 3 lists the time at which the first breakup event happens. By reducing the value of  $h_c$  the bag breaks later no matter the mesh resolution used for the solution of the Navier-Stokes equations. Also, with a given critical thickness and comparing the results for the two resolutions shown, the breakup occurs in the same spot and almost at the same time, indicating that we successfully managed to control the breakup making it almost grid independent. To summarize, in all the cases with manifold death, the breakup happens earlier than in the reference case without controlled perforation and the anticipation time depends on the critical thickness  $h_c$ .

Test case	$8192^2$ grid	$16384^2$ grid	$32768^2$ grid
Non controlled	115.0	117.5	119.2
$h_{c1} = 3\Delta_{2048}$	108.5	108.5	108.5
$h_{c2} = 3\Delta_{4096}$	112.2	112.4	112.5
$h_{c3} = 3\Delta_{8192}$	114.0	114.1	114.2

Table 3: Adimensional time at which the first breakup event occurs in the non controlled case and with three different critical thickness  $h_c$ .

### 4.3. Phase inversion problem

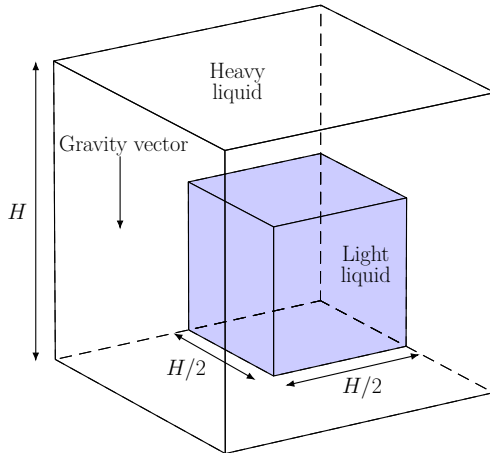


Figure 7: Configuration for the phase inversion test.

The situation of the phase inversion consists of two fluids, initially at rest, with the lighter one placed in the bottom of a box surrounded by the heavier one, see Figure 7. The outer cubic box has size  $H$ , while the inner one  $H/2$ . On the outer walls we impose a free-slip boundary condition, so that the normal velocity is zero and the tangential components obey a symmetry condition. A  $\pi/2$  static contact angle is imposed on the walls and the gravitational acceleration is  $\mathbf{g} = (0, -9.81, 0)$ . Due to gravity the lighter fluid raises and in the end will occupy the top part of the box.

In between the simple initial and final configuration, it is possible to observe many breakup and coalescence events, which in standard VOF simulations are due to both numerical and physical aspects. In particular, the role that sheets breakup plays in the lack of convergence of enstrophy has been recently pointed out in [36]. The satisfying grid convergence of primary moments, such as kinetic and mechanical energy, has already been shown in literature [37, 38, 39] and therefore here we do not provide a discussion about this aspect. In this work, however, we show that the manifold death method prevents the numerically induced breakup of thin structures and, as a consequence, the grid convergence of enstrophy and droplets size that plagues many of the literature cases is improved.

In this study, we consider moderate values of the Archimedes and Bond numbers, aiming to perform a true DNS multiphase simulation, with an accurate resolution of the fluid flow. The geometrical dimensions and the physical properties of the two fluids are reported in Table 4. Note that the properties of the lighter fluid resembles those of oil and those of the heavier one of water.

$L$	$\mu_w = \mu_o$	$\rho_w$	$\rho_o$	$\sigma$	$g$	$Ar^{1/2}$	Bo	Ca
(m)	(Pa s)	(kg m <sup>-3</sup> )	(kg m <sup>-3</sup> )	(kg s <sup>-2</sup> )	(m s <sup>-2</sup> )	-	-	-
0.1	0.01958	1000	900	0.01533	9.81	1600	640	0.4

Table 4: Physical properties and dimensionless numbers.

We introduce the following definitions for adimensional numbers and quantities

$$Ar = \frac{\rho_w(\rho_w - \rho_o)gL^3}{\mu^2}, \quad Bo = \frac{(\rho_w - \rho_o)gL^2}{\sigma}, \quad (7)$$

$$Ca = Bo/Ar^{1/2}, \quad t_c = L/U_g = 0.4515 \text{ s}.$$

The enstrophy in both fluids is obtained with

$$E_n = \frac{1}{2} \int_{\Omega} C_n \omega^2 dV, \quad (8)$$

where  $\omega = \nabla \times \mathbf{u}$  denotes the vorticity. The enstrophy is integrated over the smaller subdomain  $[0, 0.95H] \times [0, 0.95H] \times [0, H]$  to neglect regions where the dynamics is strongly affected by the presence of the walls of the box, see [36].

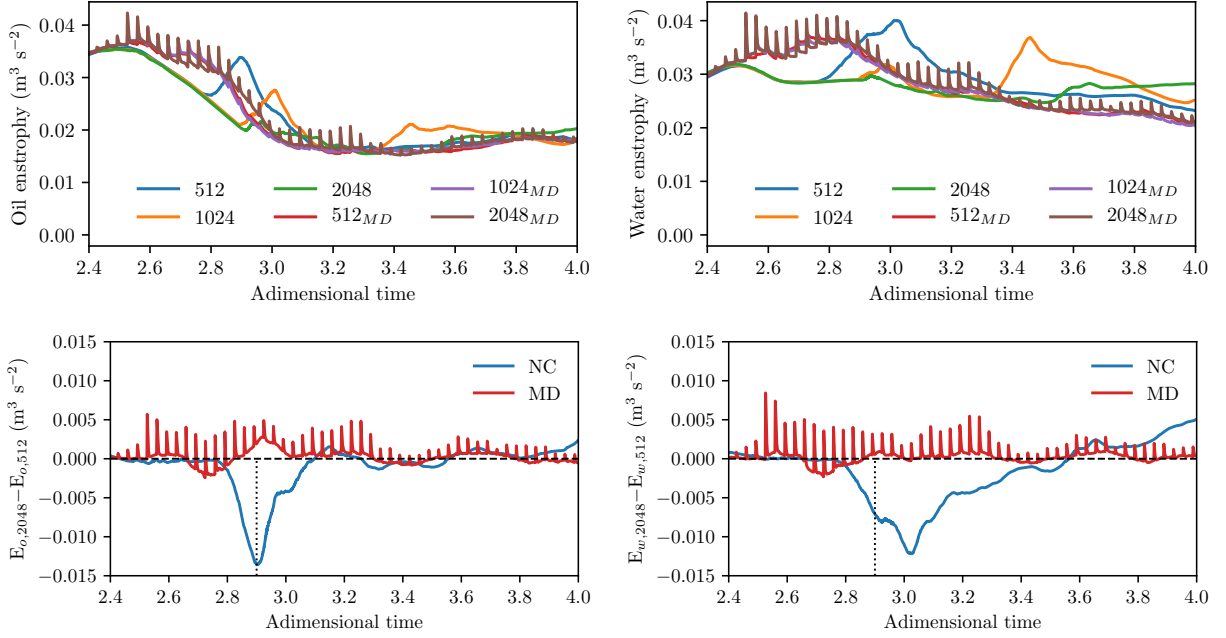


Figure 8: Top row: Oil (left) and water (right) enstrophy. Bottom row: Oil (left) and water (right) enstrophy difference between the finest and coarsest grid. The vertical dotted line at  $t^* = 2.9$  indicates when the thin sheets break in the case without controlled breakup at the coarser resolution.

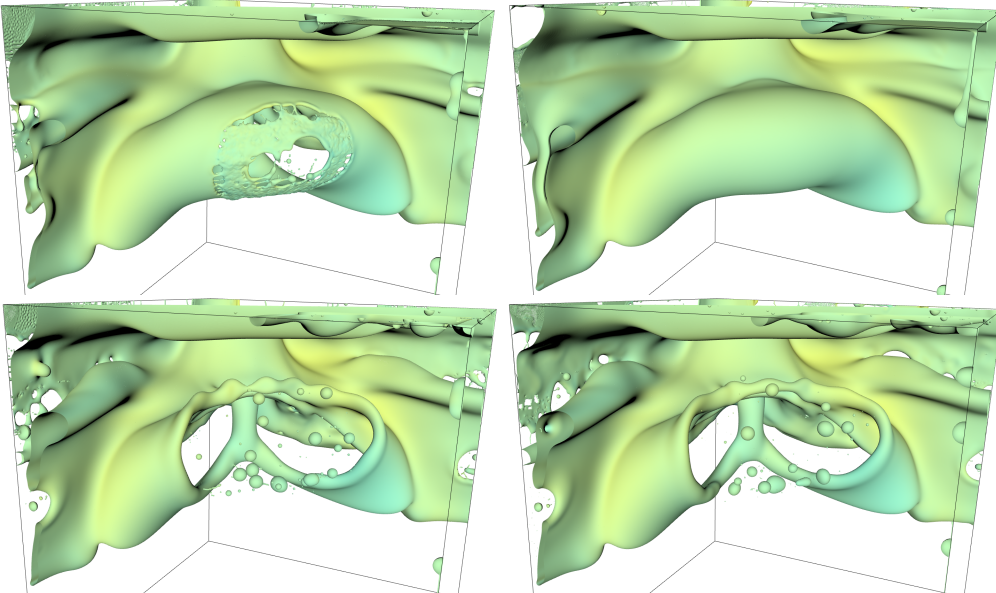


Figure 9: Thin sheet perforation and hole formation in the lighter fluid at  $t^* = 2.9$ . Top:  $512^3$  (left) and  $1024^3$  (right) grids without controlled perforations. Bottom:  $512^3$  (left) and  $1024^3$  (right) with manifold death.

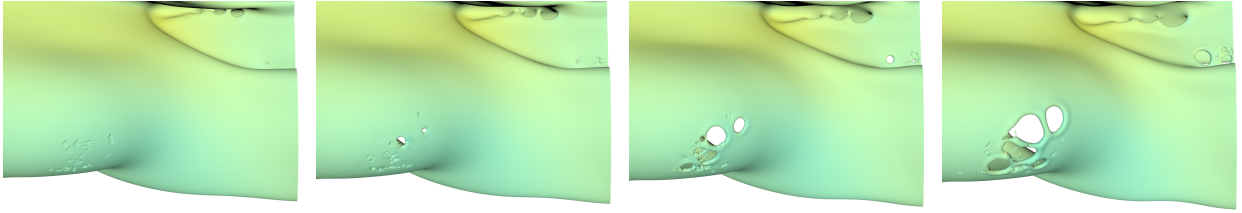


Figure 10: Evolution of the breakup of a thin sheet in the lighter fluid: close-up on the holes expansion. The holes are created by the manifold death algorithm in the first frame.

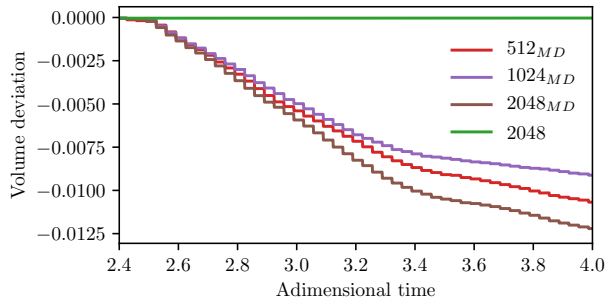


Figure 11: The volume deviation ( $V/V_0 - 1$ ) of phase 1 (lighter fluid) for the three cases with manifold death (MD) and without controlled perforation at the highest resolution.

The simulations are carried out on  $512^3$ ,  $1024^3$  and  $2048^3$  grids and the constant critical thickness is  $h_c = 3\Delta_{512}$ . The thresholds used for the refinement criteria are  $5 \cdot 10^{-3}$  and  $5 \cdot 10^{-4}$  for the velocity and volume fraction errors, respectively. Concerning the manifold death parameters, the adimensional time interval between consecutive holes formation is  $t_h^* = 0.03$  and the maximum number of holes per iteration is  $n_h = 240$ . In Figure 8 the improvements on the convergence of the oil enstrophy using the manifold death algorithm can be appreciated. In the standard case, the enstrophy peaks later using the finer grids and the local maxima decrease. Instead, when the manifold death algorithm is used to control the topology changes, the grid convergence of enstrophy is obtained. Enstrophy jumps appear when using the manifold death algorithm and their frequency is clearly  $1/t_h^*$ . They are induced by the creation of holes and we believe that their amplitude can be significantly reduced by creating holes with more realistic shapes (e.g. cylinder, torus), avoiding the sharp edges and corners of the cubic holes. Anyhow, they last for a very short period of time and therefore do not affect the overall convergence. On the bottom of the same figure, we report the enstrophy difference  $E_{2048}(t^*) - E_{512}(t^*)$  for the uncontrolled case (NC) and the one with manifold death (MD). At  $t^* = 2.9$  a large difference (almost one third of the maximum enstrophy value) can be observed between the uncontrolled cases, with more enstrophy produced using the coarser grid, while after  $t^* = 3.5$  a higher enstrophy production can be observed with the finer grid. This is due to the disruption of the sheet shown in Figure 9 and without controlled perforation its onset depends on the grid size. When using the manifold death method, the difference is much smaller and enstrophy converges.

To confirm that the cause for the non convergence upon grid refinement of enstrophy is the breakup of thin sheets in the lighter fluid, we show in Figure 9 the interface at the dimensionless time  $t^* = 2.9$  for four cases. By comparing the two pictures obtained without controlled perforation (top row) the numerical essence of the breakup is clear. In fact, at lower resolution (left) the sheet is broken and many holes and ligaments can be seen, while at a higher resolution (right) the sheet is well resolved since its thickness is larger than the grid size. On the contrary, when the manifold death algorithm is used (bottom row), at the same time the artificial holes have already destroyed the sheet in both cases and the breakup becomes grid independent. A close-up on the expansion of the holes created by the manifold death algorithm and the subsequent ligament formation is shown in Figure 10.

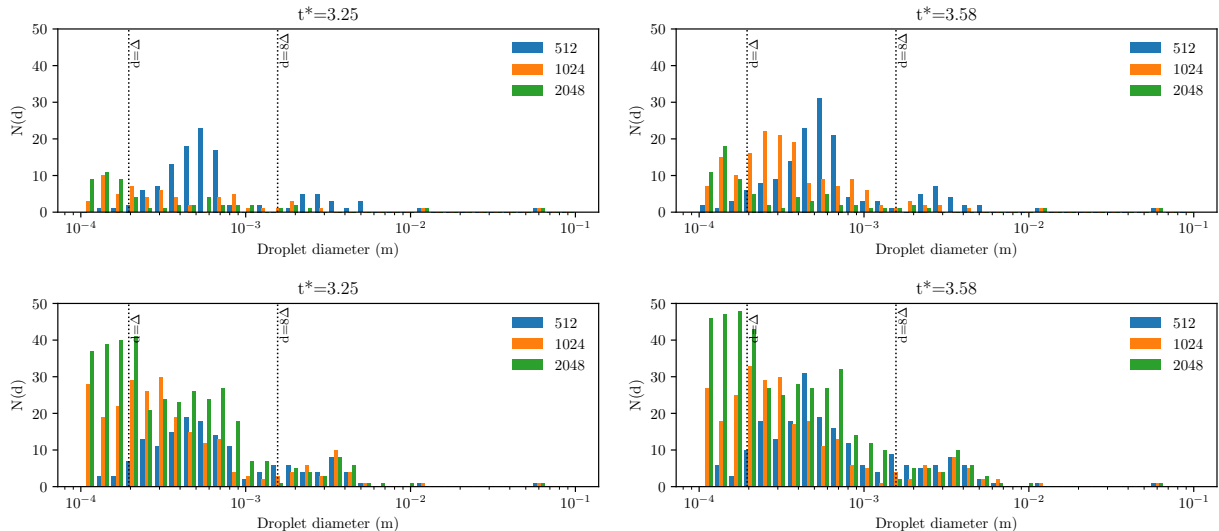


Figure 12: Droplet diameter frequency  $N(d)$  without (top) and with (bottom) controlled perforation at  $t^* = 3.25$  and  $t^* = 3.58$ . The droplet diameters are in meters and the box size is  $H = 0.1$  m.

In Figure 11, the volume deviation of fluid 1 (lighter fluid) is plotted as a function of the dimensionless time. A staircase profile is obtained for the cases with manifold death, while the mass is conserved almost exactly in the without controlled perforation. As observed for the enstrophy, the frequency of the steps is clearly  $1/t_h^*$  and their height is proportional to the mass lost (up to  $h_c^3$  for every hole created). The mass lost due to the manifold death algorithm is smaller than 1.3% and does almost not depend on the grid used for the simulation. In future works we plan to improve the method to redistribute the mass removed from the holes to the surrounding rim.

Finally, we focus on the droplet size distribution and in particular on the number of larger droplets, since they can be expected to result from both physically dominated breakup and manifold death of thin structures. In Figure 12 we compare the droplet diameter frequency  $N(d)$  obtained in the standard case (top) and with the use of manifold death (bottom) as a function of the droplet diameter. In the former, we recall that at  $t^* = 3.25$  the sheet is well resolved on the two finer grids, while on the coarser one it has been destroyed by the numerical breakup. As a consequence, more droplets have been produced using the  $512^3$  resolution. At  $t^* = 3.58$ , the sheet no longer exists also with the  $1024^3$  grid. The two larger droplets ( $d > 10^{-2}$  m) have been correctly resolved on both grids, while the frequency of the smaller ones shows similar profiles, with a shift towards the left (smaller droplets) when the finer mesh is used. This confirms the numerical nature of the breakup. With controlled perforation, the number of trustworthy droplets on the right of the dashed line ( $d > 8\Delta_{512}$ ) is similar for the three grids and at both times. Moreover, when the mesh size decreases, more small droplets (in the untrustworthy region  $d < \Delta_{512}$ ) are again collected.

## 5. Conclusions

We have described a new method to detect thin structures and to create holes depending only on the value of the critical thickness  $h_c$ . We have performed a simple single vortex test to prove the ability to locate thin ligaments of thickness  $h_c$  independently on the grid resolution. The axisymmetric secondary atomization and the three-dimensional phase inversion tests show the improvements in terms of grid convergence that the method can provide to the study of complex multiphase simulations. The findings of this study suggest that using an algorithm to induce in a controlled way the breakup of thin structures is necessary to obtain grid independence of the droplet size distribution and second order moments such as enstrophy. Future work will concentrate on improving the numerical hole formation, for example by re-distributing the mass near the holes rather than removing it, to better conserve mass and energy.

## Acknowledgements

The authors benefited from the ERC grant TRUFLOW. The project also benefited from the PRACE grant TRUFLOW number 2020225418 for a large number of CPU hours in 2021. We are grateful for access to the computational facilities TGCC granted by GENCI under project number A0092B07760. We thank the support of the CSCS Supercomputer Centre through the grant s1136, involving the time in the Piz Daint supercomputer.

## References

- [1] E. Villermaux. Fragmentation versus cohesion. *Journal of Fluid Mechanics*, 898, 2020.
- [2] D. Lohse and E. Villermaux. Double threshold behavior for breakup of liquid sheets. *Proceedings of the National Academy of Sciences*, 117(32):18912–18914, 2020.
- [3] J.N. Israelachvili. *Intermolecular and surface forces*. Academic Press, New York, 1992. Second edition.
- [4] A. Vrij. Possible mechanism for the spontaneous rupture of thin, free liquid films. *Discussions of the Faraday Society*, 42:23–33, 1966.
- [5] E. Ruckenstein and R.K. Jain. Spontaneous rupture of thin liquid films. *Journal of the Chemical Society, Faraday Transactions 2: Molecular and Chemical Physics*, 70:132–147, 1974.
- [6] B.P. Radoev, A.D. Scheludko, and E.D. Manev. Critical thickness of thin liquid films: theory and experiment. *Journal of colloid and interface science*, 95(1):254–265, 1983.
- [7] W.W. Zhang and J.R. Lister. Similarity solutions for Van der Waals rupture of a thin film on a solid substrate. *Physics of Fluids*, 11(9):2454–2462, 1999.
- [8] D. Moreno-Boza, A. Martínez-Calvo, and A. Sevilla. Stokes theory of thin-film rupture. *Physical Review Fluids*, 5(1):014002, 2020.
- [9] L. Opfer, I.V. Roisman, J. Venzmer, M. Klostermann, and C. Tropea. Droplet-air collision dynamics: Evolution of the film thickness. *Phys. Rev. E*, 89(1):013023, 2014.
- [10] S. Poulain, E. Villermaux, and L. Bourouiba. Ageing and burst of surface bubbles. *Journal of fluid mechanics*, 851:636–671, 2018.
- [11] Y. Ling, D. Fuster, S. Zaleski, and G. Tryggvason. Spray formation in a quasiplanar gas-liquid mixing layer at moderate density ratios: a numerical closeup. *Physical Review Fluids*, 2(1):014005, 2017.
- [12] G.G. Agbaglah. Breakup of thin liquid sheets through hole–hole and hole–rim merging. *Journal of Fluid Mechanics*, 911, 2021.
- [13] J.A. Sethian. *Level set methods and fast marching methods: evolving interfaces in computational geometry, fluid mechanics, computer vision, and materials science*, volume 3. Cambridge university press, 1999.
- [14] L. Zhao, H. Khuc, J. Mao, X. Liu, and E. Avital. One-layer particle level set method. *Computers & Fluids*, 170:141–156, 2018.
- [15] C. Wang, W. Wang, S. Pan, and F. Zhao. A local curvature based adaptive particle level set method. *Journal of Scientific Computing*, 91(1):1–20, 2022.
- [16] H.Z. Yuan, C. Shu, Y. Wang, and S. Shu. A simple mass-conserved level set method for simulation of multiphase flows. *Physics of Fluids*, 30(4):040908, 2018.
- [17] G. Tryggvason, B. Bunner, A. Esmaeeli, D. Juric, N. Al-Rawahi, W. Tauber, J. Han, S. Nas, and Y.J. Jan. A front-tracking method for the computations of multiphase flow. *Journal of computational physics*, 169(2):708–759, 2001.
- [18] M. Jemison, M. Sussman, and M. Shashkov. Filament capturing with the multimaterial moment-of-fluid method. *Journal of Computational Physics*, 285:149–172, 2015.
- [19] R.M. Chiodi. *Advancement of numerical methods for simulating primary atomization*. Cornell University, 2020.
- [20] F. Henri, M. Coquerelle, and P. Lubin. Geometrical level set reinitialization using closest point method and kink detection for thin filaments, topology changes and two-phase flows. *Journal of Computational Physics*, 448:110704, 2022.
- [21] J. Lu and G. Tryggvason. Direct numerical simulations of multifluid flows in a vertical channel undergoing topology changes. *Physical Review Fluids*, 3(8):084401, 2018.
- [22] C. Focke, M. Kuschel, M. Sommerfeld, and D. Bothe. Collision between high and low viscosity droplets: direct numerical simulations and experiments. *International journal of multiphase flow*, 56:81–92, 2013.
- [23] P. Kant, C. Pairetti, Y. Saade, S. Popinet, S. Zaleski, and D. Lohse. Bags mediated film atomization in a cough machine. *arXiv preprint arXiv:2202.13949*, 2022.
- [24] G. Tryggvason, R. Scardovelli, and S. Zaleski. *Direct numerical simulations of gas-liquid multiphase flows*. Cambridge Univ. Press, 2011.
- [25] S. Popinet. A quadtree-adaptive multigrid solver for the Serre–Green–Naghdi equations. *Journal of Computational Physics*, 302:336–358, 2015.
- [26] J.A. Van Hooft, S. Popinet, C.C. Van Heerwaarden, S.J.A. Van der Linden, S.R. de Roode, and B.J.H. Van de Wiel. Towards adaptive grids for atmospheric boundary-layer simulations. *Boundary-layer meteorology*, 167(3):421–443, 2018.
- [27] S. Popinet. Numerical models of surface tension. *Annu. Rev. Fluid Mech.*, 50:49–75, 2018.
- [28] M. Galassi, J. Davies, J. Theiler, B. Gough, G. Jungman, P. Alken, M. Booth, F. Rossi, and R. Ulerich. *GNU scientific library*. Network Theory Limited, 2002.

- [29] J. Zhang, M. Ni, and J. Magnaudet. Three-dimensional dynamics of a pair of deformable bubbles rising initially in line. Part 1. Moderately inertial regimes. *Journal of Fluid Mechanics*, 920, 2021.
- [30] G.I. Taylor and D.H. Michael. On making holes in a sheet of fluid. *Journal of fluid mechanics*, 58(4):625–639, 1973.
- [31] J.B. Bell, P. Colella, and H.M. Glaz. A second-order projection method for the incompressible Navier–Stokes equations. *Journal of computational physics*, 85(2):257–283, 1989.
- [32] E. Aulisa, S. Manservigi, R. Scardovelli, and S. Zaleski. A geometrical area-preserving Volume-of-Fluid advection method. *Journal of Computational Physics*, 192(1):355–364, 2003.
- [33] M. Pilch and C.A. Erdman. Use of breakup time data and velocity history data to predict the maximum size of stable fragments for acceleration-induced breakup of a liquid drop. *International journal of multiphase flow*, 13(6):741–757, 1987.
- [34] D.R. Guddenbecher, C. López-Rivera, and P.E. Sojka. Secondary atomization. *Experiments in Fluids*, 46(3):371–402, 2009.
- [35] F. Marcotte and S. Zaleski. Density contrast matters for drop fragmentation thresholds at low Ohnesorge number. *Phys. Rev. Fluids*, 4:103604, 2019.
- [36] T. Sayadi, S. Zaleski, S. Popinet, V. Le Chenadec, and S. Vincent. A convergence study of the one-fluid formulation in a phase inversion application at moderate Reynolds and Weber numbers. In *Turbulence and Interactions: Proceedings of the TI 2018 Conference, June 25-29, 2018, Les Trois-Îlets, Martinique, France*, volume 149 of *Notes Numer. Fluid Mech. (NNFM)*, page 80. Springer Nature, 2021.
- [37] S. Vincent, J.-P. Caltagirone, and D. Jamet. Test-case n° 15: phase inversion in a closed box (PC). *Multiphase Sci. Technol.*, 16:101–104, 2004.
- [38] M. Saeedipour, S. Vincent, and J.-L. Estivalezes. Toward a fully resolved volume of fluid simulation of the phase inversion problem. *Acta Mechanica*, pages 1–20, 2021.
- [39] J.-L. Estivalezes, W. Aniszewski, F. Auguste, Y. Ling, L. Osmar, J.-P. Caltagirone, L. Chirco, A. Pedrono, S. Popinet, A. Berlemont, et al. A phase inversion benchmark for multiscale multiphase flows. *Journal of Computational Physics*, 450:110810, 2022.